Niobium speciation in minerals revealed by L2,3-edges XANES spectroscopy

Quentin Bollaert, Mathieu Chassé, Hebatalla Elnaggar, Amélie Juhin, Alexandra Courtin, Laurence Galoisy, Cécile Quantin, Marius Retegan, Delphine Vantelon, Georges Calas

Title: Niobium speciation in minerals revealed by L2,3-edges XANES spectroscopy
Manuscript Number: 8293R
Authors: Quentin Bollaert, Sorbonne University Mathieu Chassé, Sorbonne University Hebatalla Elnaggar, Sorbonne University Amélie Juhin, Sorbonne University Alexandra Courtin-Nomade, University of Paris-Saclay Laurence Galoisy, Sorbonne University Cécile Quantin, University of Paris-Saclay Marius Retegan, ESRF - European Synchrotron Radiation Facility Delphine Vantelon, Georges Calas, Sorbonne University

Word Count: 8,718 words

Niobium speciation in minerals revealed by $L_{2,3}$-edges XANES spectroscopy

Authors: Bollaert Quentin[1], Chassé Mathieu[1], Elnaggar Hebatalla[1], Juhin Amélie[1], Courtin-Nomade Alexandra[2], Galoisy Laurence[1], Quantin Cécile[2], Retegan Marius[3], Vantelon Delphine[4], Calas Georges[1]

Affiliations:

[1]Sorbonne Université, Institut de Minéralogie, de Physique des Matériaux et de Cosmochimie, 4 place Jussieu, Paris, 75005, France

[2]Université Paris-Saclay, UMR 8148 GEOPS, 91405 Orsay Cedex, France

[3]European Synchrotron Radiation Facility, 71 Av. des Martyrs, Grenoble, 38043, Auvergne Rhône Alpes, France

[4]Synchrotron SOLEIL, L'Orme des Merisiers, Saint-Aubin, BP 48 91192 Gif-sur-Yvette Cedex, France

ABSTRACT

The complexity of niobium (Nb) mineralogy, dominated by more than one hundred oxides of similar crystal chemistry, makes it particularly challenging to determine Nb speciation in minerals. Here, we describe the first Nb $L_{2,3}$-edges X-ray absorption near-edge structure (XANES) data on Nb-bearing minerals and synthetic oxides relevant to geological contexts. The interpretation of Nb $L_{2,3}$-edges XANES spectra in light of crystal-field theory mirrors the sensitivity of spectra to the local site symmetry and the electronic configuration around Nb atoms. Crystal-field multiplet simulations give estimates of the 10*Dq* crystal-field parameter of Nb^{5+}, ranging from 2.8 to 3.9 eV depending on Nb coordination and Nb–O distances. In particular, the 10*Dq* vs. R^{-5} relationship (where R represents the average Nb–O bond distance) is observed for octahedrally-coordinated Nb, as expected in a point-charge model. Complementary ligand-field multiplet simulations provide evidence of charge transfer between Nb and O. The Nb–O bonds show an equivalent mixing between ionic and covalent character unlike more ionic 3*d* metal–O bonds. These interpretations provide information on the mechanisms by which Nb^{5+} substitutes for Fe^{3+}, Ti^{4+} or Ce^{4+} in oxides common in environmental contexts. Whereas the substitution of Nb^{5+} for Ce^{4+} does not modify the local structure of the cation site in cerianite, the substitution of Nb^{5+} for Ti^{4+} in rutile and anatase results in an increase of the cation-ligand distance and a decrease in the symmetry of the cation site. Conversely, the substitution of Nb^{5+} for Fe^{3+} in hematite and goethite results in a smaller cation site distortion. Our study demonstrates the usefulness of Nb $L_{2,3}$-edges XANES spectroscopy to constrain Nb speciation in minerals with direct relevance for understanding the processes that can concentrate this critical metal at economic levels.

Keywords: Niobium, XANES, multiplet, 10*Dq*, local structure, speciation

INTRODUCTION

Niobium (Nb) is a typical critical element (European Commission 2020). It is intensively used by industry to produce superalloys, superconducting magnets and catalysts (Schulz et al. 2017). In the frame of the environmental transition, Nb-based materials are also valued for their large range of innovative properties that result from structural defects (Ismael 2020, Ma et al. 2020). This multitude of applications is expected to increase the demand in the coming years. This economic importance is combined with the scarcity of Nb deposits. The low concentration of Nb on Earth, ca. 12 ppm in the upper continental crust (Rudnick and Gao 2014), and its geochemical properties limit the incorporation of Nb into most common rock-forming minerals. Under oxygen fugacities relevant to lithospheric and surficial environments, Nb occurs only as Nb^{5+} (Cartier et al. 2015) with the electronic configuration [Kr] $4d^0$. Its high valence relative to its ionic radius (0.64 Å in octahedral coordination, i.e. Shannon 1976) makes Nb one of the high-field-strength elements (HFSE) along with Zr, Sn, Hf, Ta, Pb, Th and U. Niobium concentrates in silicic melts during partial melting and fractional crystallization until the late precipitation of Nb minerals of the pyrochlore and columbite supergroups (Linnen and Cuney 2005). During weathering, Nb is among the most immobile elements (Hill et al. 2000) due to the resistance of primary Nb minerals to alteration. It is consequently used for mass-balance calculations (Kurtz et al. 2000) and environmental studies (Nabi et al. 2021) although the presence of organic ligands, which can increase Nb solubility, challenges this approach (Friis and Casey 2018). Such geochemical behavior is basic to the formation of world-class lateritic Nb deposits, as a consequence of a significant residual enrichment during lateritic weathering of primary deposits, typically by an order of magnitude relative to the parent rock (Mitchell 2015).

Niobium is octahedrally coordinated with oxygen ligands in ca. 85 % of Nb minerals (Waroquiers et al. 2017). The most abundant phases are multicomponent oxides with the general formula AB_2O_6 (columbite-group minerals: e.g. columbite, euxenite, aeschynite) and $A_{2-x}B_2O_7$ (pyrochlore-group minerals: pyrochlore, betafite, samarskite). The eight-fold coordinated A-

site, a square antiprism, is occupied by rare-earth elements (REE), Ca, U, Th, Fe, while the octahedral B-site is occupied by Ti, Nb, Ta and W and forms double chains in a zigzag pattern by sharing at least two edges with neighboring octahedra (Ewing 1975). Due to strong interionic repulsion, most NbO_6 octahedra are distorted (Kunz and Brown 1995). Metamictization is common due to the presence of radioactive elements (Zietlow et al. 2017). It can form local structures made of corner-sharing octahedra at the expense of the edge-sharing linkages observed in the crystalline oxides (Ewing 1975). Unambiguous identification of Nb minerals is needed to understand geological and geochemical processes concentrating Nb such as magmatic differentiation (Walter et al. 2018; Lee et al. 2006), metasomatic events (Wu et al. 2021) and supergene weathering (Lottermoser and England 1988; Wall et al. 1996). However, the similar crystal chemistry and metamictization of Nb minerals make the analysis of Nb speciation using X-ray diffraction analyses challenging.

Niobium is also found as a minor or trace element in minerals. Hydrothermal events can result in the formation of amorphous Fe oxides containing low amounts of Nb (Wu et al. 2021). In metasomatized mantle peridotites, rutile may host more than 95 % of the Nb budget (Kalfoun et al. 2002). Niobium can also be enriched in Fe and Ti oxides that occur as veinlets or degradation products in laterites (Lottermoser and England 1988; Giovannini et al. 2017). These oxides highlight the capacity of Nb^{5+} to substitute for cations such as Ti^{4+}, Sn^{4+}, W^{6+}, Ce^{4+} and Fe^{3+} in various minerals (Černý and Ercit 1989; Giovannini et al. 2017), which also hinders the determination of Nb speciation in such geological contexts.

Here, we report the first analysis of Nb $L_{2,3}$-edges XANES spectra using a selected set of Nb minerals (fluorcalciopyrochlore, hydropyrochlore, niocalite, Nb perovskite, columbite) and synthetic oxides (hematite, goethite, rutile, anatase, cerianite, lueshite and Nb_2O_5). A few studies have been published on synthetic Nb oxides and fluorides (Sugiura et al. 1988; Kubouchi et al. 2012; Wang et al. 2018). The objective of this work is twofold. (i) Relate spectral properties to the local structure around Nb in crystalline references. Crystal-field and ligand-field multiplet (CFM

and LFM) calculations provide the first data on crystal-field parameters and Nb–O bond covalence in minerals. This CFM and LFM approach has proven useful to model Fe bioavailability and mobility in terrestrial and subsurface environments (Bhattacharyya et al. 2019) and V speciation in fresnoite (Höche et al. 2013). (ii) Investigate the processes by which Nb substitutes for Fe, Ti and Ce in Nb-substituted oxides. These materials serve as models for model major Nb-bearing oxides found in geological contexts and used in industry. Overall, this first study on Nb speciation in mineralogical contexts demonstrates how the sensitivity of Nb $L_{2,3}$-edges XANES spectroscopy can be used to better characterize and understand Nb mineralogy. Deciphering Nb speciation will improve our understanding of Nb enrichment in primary and lateritic deposits and may help to diversify the range of primary sources and to upgrade the efficiency of ore processing (Černý and Ercit 1989).

MATERIALS AND METHODS

Mineral synthesis procedures

Niobium-substituted Fe oxides (1 wt% Nb). The synthesis of Nb-bearing goethite (α-FeOOH) has been adapted from the hydrothermal synthesis of Sc-bearing Fe oxides at 70 °C (Chassé et al. 2017). Nb-bearing goethite was converted into Nb-bearing hematite (α-Fe_2O_3) by dehydroxylation at 300 °C for 2 h. The solid was washed using H_2SO_4 in order to remove potential adsorbed Nb species and poorly-crystallized material.

Niobium-substituted Ti oxides (5 wt% Nb). The synthesis of Nb-bearing anatase (TiO_2) has been carried out using a sol-gel method at moderate temperature (Dufour et al. 2012). Niobium-bearing rutile (5 wt%) was obtained by heating Nb-bearing anatase (5 wt%) at 700 °C for 3 hours. Niobium-bearing anatase was also synthesized with 1 and 10 wt% Nb following this procedure.

Niobium-substituted cerianite (1 wt% Nb). Niobium-bearing cerianite was synthesized using a high temperature solid-state reaction at 1,300 °C by homogenizing CeO_2, Nb_2O_5 and Nd_2O_3 powders (Olegário et al. 2013).

Lueshite. This reference material was obtained by following a hydrothermal synthesis procedure at 200 °C over 24 h based on the experimental protocol of Gouget et al. (2019).

Analytical methods

Powder X-ray diffraction (XRD) analyses. The successful completion of the syntheses was verified by X-ray diffraction analysis. X-ray diffraction was performed using a PANALYTICAL X'pert Pro MPD diffractometer. Measurements were carried out in Bragg-Brentano geometry using a Co Kα anode in order to minimize the X-ray absorption of Fe in hematite and goethite. Data were recorded with an X'Celerator detector between 3 °2θ and 90 °2θ with 0.017 ° steps. The incident beam mask was fixed at 20 mm and the Soller slits at 0.04 rad. Total counting time of measurement was 3 hours per sample. The crystal structure of synthetic compounds was checked using the International Centre for Diffraction Data (ICDD) references (PDF-2 database). No secondary niobian phase was detected on the XRD patterns of Nb-bearing Fe, Ti and Ce oxides confirming that the Nb ions were incorporated into the crystal lattice and substituted for Fe, Ce and Ti (Supplemental Figs. S1 and S2).

Single crystal XRD. Single-crystal X-ray diffraction data were acquired on natural Nb reference materials on an Agilent Diffraction Xcalibur-S diffractometer equipped with a Sapphire CCD-detector with Mo K-α1 radiation (λ = 0.71073 Å, graphite monochromator) at 293 K. Data reduction, cell refinement and space group determination were performed using the CrysAlisPro software.

Electron microprobe (EMP) analyses. Electron microprobe (EMP) analyses were used to determine the crystal chemistry of the Nb reference materials sourced from the mineralogical collections. Analyses were conducted on a CAMECA SX Five electron probe at the CAMPARIS facility (Sorbonne Université, Paris). After checking the homogeneity of the samples, two to seven spots were probed on each sample at 15 kV and 40 nA for the major elements and at 15 kV and 299 nA for minor and trace elements. Wavelength-dispersive spectroscopy analyses were performed using the following standards: albite for Na, diopside for Mg, Si and Ca, orthoclase for Al and K,

147 $MnTiO_3$ for Mn and Ti, hematite for Fe, $BaSO_4$ for Ba, topaz for F, $LiNbO_3$ for Nb, metallic Ta for
148 Ta, SrSi for Sr, zircon for Zr, galena for Pb, monazite for Th, uraninite for U, and allanite-(Y) for Y,
149 La, Ce, Nd.

150 **X-ray absorption spectra acquisition.** Niobium $L_{2,3}$-edges XANES spectra were recorded
151 on the LUCIA beamline of the SOLEIL synchrotron radiation facility (Gif-sur-Yvette, France)
152 operating with a storage ring current of 450 mA and energy of 2.75 GeV (Vantelon et al. 2016). A
153 double crystal Si(111) monochromator crystal was used with an energy resolution of 0.25 eV at
154 2400 eV (Schaefers et al. 2007). The monochromator was calibrated at the energy of the Nb L_3-edge
155 using Nb_2O_5. Due to the high Nb contents in Nb minerals, the spectra were recorded on cellulose-
156 diluted pellets before being mounted on a holder. Pure pellets were used for synthetic Nb-
157 substituted samples. Data were obtained between 2300 and 2550 eV at room temperature, under
158 vacuum, in fluorescence mode. Energy steps were (2, 0.2, 1, 0.2, 1) eV for energy ranges of (2300–
159 2350), (2350–2400), (2400–2455), (2455–2490) and (2490–2550) eV, respectively, with a 1 s
160 integration time. Two measurements per sample were sufficient to get adequate signal-to-noise
161 ratios and to check the reproducibility of the edge features.

162 **Data processing and simulations**

163 **X-ray absorption data processing.** Processing of the data was achieved using the Larch
164 software (Newville 2013). The MBACK normalization algorithm was applied to prevent distortion
165 in the XANES data and preserve the branching ratio (Weng et al. 2005). This method applies a
166 single smooth background function over the entire $L_{2,3}$-edges data range rather than normalizing
167 each edge independently. The normalization function is a first order Legendre polynomial
168 (Supplemental Fig. S3) and the edge energy chosen as the input parameter of the MBACK function
169 implemented in Larch is 2371 eV. The spectra of Nb-substituted hematite, Nb-substituted goethite,
170 lueshite, and niocalite were trimmed beyond 2475 eV because the S K-edge hides the high-energy
171 features of the Nb L_2-edge.

172 Niobium $L_{2,3}$-edges XANES features were fitted using three pseudo-Voigt functions in

order to quantitatively compare and retrieve differences in the three features between the spectra. The continuum background was removed using an error function with fixed inflection points (2373.0 and 2467.0 eV) and large width (ca. 8 eV) to reproduce the slow onset of the electronic continuum (Brotton et al. 2007). No agreement or convention exists regarding the parameters of the background functions (Henderson et al. 2014) but similar procedures have been applied to Fe $L_{2,3}$-edges (Bourdelle et al. 2013) and Zr $L_{2,3}$-edges (Jollivet et al. 2013). An error function was preferred over the commonly-used arctangent because its width is related to the instrumental resolution rather than to the lifetime of the excited state, which is not known a priori. Because the best mathematic fits were obtained for a relative weight of Lorentzian to Gaussian components between 0.8 and 1.0 depending on the spectra, this parameter was fixed to 0.9 in all fits for comparative purposes.

Crystal-field and ligand-field multiplet calculations. Simulations of the Nb $L_{2,3}$-edges spectra were performed using the Crispy software as implemented in the Quanty library (Haverkort 2016; Retegan 2019). Two approaches were tested to reproduce the spectral features. The first is a CFM calculation which takes into account the crystal-field effects acting on Nb. Ligand-field multiplet calculations offer a more comprehensive model by including the ligand-to-metal charge transfer, i.e. by mixing in the ground state the $4d^0$, $4d^1\underline{L}^1$, $4d^2\underline{L}^2$, $4d^3\underline{L}^3$ configurations through a hybridization Hamiltonian (more details on this notation are provided in the Supplemental Material).

Crystal- and ligand-field multiplet calculations both require the specific input parameters. To account for the lifetime broadening, Lorentzian functions with a full width at half-maximum of 1.66 eV and 1.87 eV for the L_3 and L_2-edges were used to simulate the features (Krause and Oliver 1979). The experimental Gaussian broadening was set to ca. 1.5 eV to best reproduce the experimental spectra. The simulations of the experimental spectra were carried out by finding the best scaling factors for the Slater-Condon integrals that best account for direct and exchange interactions between the 2*p*–4*d* orbitals (F^2_{pd} = 2.680 eV, G^1_{pd} = 1.627 eV and G^3_{pd}= 0.946 eV for

the free ion). The reduction of these values modifies the relative intensity of the features. The values of the 4*d* and 2*p* spin-orbit coupling parameters were kept close to the atomic values of 0.124 eV and 63.97 eV. The crystal-field splitting parameter (10*Dq*) was chosen to best reproduce the energy difference between the two features, which corresponds to the splitting of the final state of the *d* orbitals. The extra parameters required for LFM calculations are the hybridization strength V_{mix} (V_{t2g}, V_{eg}), the configuration-averaged energies of the charge transfer configuration (E($4d^1\underline{L}^1$)–E($4d^0$)) Δ, the core-hole potential U_{dc} and the average Coulomb interaction energies of a corresponding electron pair U_{dd}. Detailed explanations of these parameters and their influence on the spectral shapes are given in the Supplemental Material (Supplemental Fig. S7).

RESULTS

Characteristics of niobium $L_{2,3}$-edges XANES spectra

The Nb $L_{2,3}$-edges XANES spectra (Fig. 1) are characterized by a split edge feature with two peaks (A and B features) followed by a peak of lower intensity, ca. 10 eV after the edge (C feature), as reported for other Nb-bearing materials (Sugiura et al. 1988; Wang et al. 2018). The energy of the L_3-edge features (A_3, B_3, C_3) varies around ca. 2372, 2376 and 2387 eV, respectively (Fig. 1a). The energy of the L_2-edge features (A_2, B_2, C_2) varies around ca. 2466, 270 and 2481 eV, respectively (Fig. 1b). At the L_3-edge, the energy position and width of the A_3 feature are stable, whereas that of B_3 varies among the reference materials. Niocalite, Nb-substituted hematite and Nb-substituted goethite spectra show narrower B_3 features than the other reference materials. In contrast, the wide B_3 feature of the Nb perovskite spectrum shows a shoulder at high energy (B'_3 at 2379–2380 eV, Fig 2b). The intensity ratio between the A_3 and B_3 features (A_3/B_3) varies but remains larger than 1 except in the Nb-substituted cerianite L_3-edge spectrum. In all compounds, C_3 is of lower intensity than A_3 and B_3 with limited variation in position and width. Similar trends are observed at the L_2-edge.

Analysis of the niobium $L_{2,3}$-edges XANES spectra

Variation of the edge splitting. The ΔE parameter, corresponding to the energy splitting between the A and B features, ranges from ca. 2.6 to 4.0 eV at the L_3-edge and from ca. 2.3 to 4.0 eV at the L_2-edge (Table 2). The Nb pervoskite, lueshite, fluorcalciopyrochlore and hydropyrochlore spectra have the largest ΔE values (ranging from ca. 3.6 to 4.0 eV). Most spectra have ΔE values between ca. 3.1 and 3.5 eV except for the Nb-substituted cerianite spectrum (ca. 2.6 and 2.3 eV at L_3- and L_2-edges, respectively). Overall, the energy splitting at the L_3-edge follows the same trend ($R^2 = 0.94$) as the energy splitting at the L_2-edge (Supplemental Fig. S6a).

Variation of the intensity ratio. The intensity ratio (I_A/I_B) varies between ca. 0.8 and 2.1. It is higher at the L_2-edge (1.43) than at the L_3-edge (1.07). In most compounds, it ranges between ca. 1.0–1.2 and 1.4–1.6 at the L_3- and L_2-edge, respectively (Table 2). Intensity ratios of Nb-substituted cerianite and Nb_2O_5 spectra are below 1 at the L_3-edge. There is a strong positive correlation of this parameter between the two edges ($R^2 = 0.95$, Supplemental Fig. S6b).

Variation of the bandwidth. The ratio of the full width at half maximum of feature B with respect to feature A ($FWHM_{B/A}$), ranges between ca. 1.0 and 2.2 for both edges. The spectra of Nb-substituted goethite and hematite (Fig. 2c) have the lowest $FWHM_{B/A}$ values (ca. 1.1 and 1.4 at the L_3- and L_2-edge, respectively). Most spectra exhibit intermediate $FWHM_{B/A}$ values (ca. 1.4–1.7 and ca. 1.6–1.9 at the L_3- and L_2-edge, respectively). The Nb perovskite spectrum (Fig. 2b) stands out by its high $FWHM_{B/A}$ value (ca. 2.1 and 2.4 at the L_3-and L_2-edges, respectively). Niobium-substituted anatase spectra (Fig. 2d) are also characterized by high $FWHM_{B/A}$, especially at the L_2-edge (ca. 1.8–1.9 eV). On average, the width ratios at the L_3-edge (1.54) are smaller than those at the L_2-edge (1.73). The $FWHM_{B/A}$ parameter is correlated between the two edges ($R^2 = 0.93$), after excluding the lueshite spectra, which deviate from the general trend (Supplemental Fig. S6c).

Multiplet calculations

Crystal-field multiplet calculations. The spectral features of Nb-substituted cerianite and

hematite are well reproduced by considering Nb in a regular polyhedron (O_h) (Figs. 3a and 3b) with crystal field values of 2.8 and 3.7 eV, respectively (Table 3). The spectra of hydropyrochlore and Nb perovskite are best modeled with a 10*Dq* value of 3.9 eV, which reproduces the splitting between the features (Figs. 3c and 3d). Nonetheless, the B' features of low intensity at 2379–2380 eV do not appear. The good reproduction of the intensity ratios of the spectra for Nb-substituted cerianite, hematite and hydropyrochlore results from the reduction of the Slater-Condon integrals to 50 %, an indication of the equivalent mixing between ionic and covalent character in the Nb–O bonds. The high intensity ratios of Nb perovskite spectra (Table 2) are reproduced with the reduction of the Slater-Condon integrals to 35 %.

Ligand-field multiplet calculations. We calibrated our calculations using Nb-substituted hematite, which exhibits the simplest spectral features. Charge-transfer parameters (U_{dc}, U_{dd}, Δ, V_{mix}) were chosen (Table 4) in agreement with the calculations done on Ti^{4+} ($3d^0$)-compounds (Okada and Kotani 1993). The intensity of the features of Nb-substituted hematite spectra is improved and the C feature at ca. 2385 eV is reproduced when charge transfers are considered (Fig. 4). We also attempted to reproduce the B' features in the spectra of hydropyrochlore and Nb perovskite by investigating the influence of the hybridization strength (V_{mix}) on the spectral shapes. Using the same charge-transfer parameters, the LFM calculation fails to explain the coexistence of both B' and C features in hydropyrochlore and Nb perovskite (Fig. 5).

DISCUSSION

$L_{2,3}$-edges XANES spectroscopy mirrors the Nb electronic environment

Spectral energy splitting, interatomic distances and site symmetry. Niobium $L_{2,3}$-edges correspond to transitions to empty 4*d* states, making them sensitive to crystal-field effects. In the frame of crystal-field theory and given that O^{2-} is the ligand of Nb^{5+} in all of the reference materials, ΔE is correlated with the 10*Dq* crystal field parameter, mirroring Nb^{5+} site geometry and ligand distances.

The ΔE values range between 3.3 and 4.0 eV for octahedrally-coordinated Nb^{5+}. The ΔE

variability among octahedral reference materials is correlated with the average interatomic distances ($R^2 = 0.84$), as expected from the relationship between $10Dq$ and R^{-5} (Fig. 6) in a point-charge model (Burns 1993). Nonetheless, Nb-substituted Ti oxides deviate from this trend, showing distinct Nb–O and average Ti–O distances.

Among octahedral Nb reference materials, the spectra of Nb_2O_5 show the lowest ΔE values (3.06 and 3.28 eV at the L_2- and L_3-edge, respectively), slightly higher than previously reported (2.6 and 2.8 eV; i.e Sugiura et al. 1988). Nb_2O_5 powders may differ from each other in the nature and proportion of the polymorphs they contain (Pilarek et al. 2017). Unfortunately, the material investigated by Sugiura was not characterized by XRD. Our Nb_2O_5 reference consists of several polymorphs in equivalent proportions, of which two crystallize in monoclinic (ca. 90 % of NbO_6 octahedra and 10 % NbO_5 polyhedra: Andersson 1967) and orthorhombic (NbO_5 and NbO_7 polyhedra; i.e. Waring et al. 1973) structures (Supplemental Fig. S2c). These structural differences may explain a lower splitting as compared to the other octahedrally-coordinated Nb reference materials.

The ΔE value of the cerianite spectrum in which Nb is in a cubic site, is 6/9–7/9 times smaller compared to octahedral reference materials (Table 2). Crystal-field splitting values are lower than expected in cubic coordination ($10Dq_c$ is 8/9 of $10Dq_o$). Though not detected by XRD (Supplemental Fig. S2b), the occurrence of trace amounts of tetrahedrally-coordinated fergusonite-(Ce) could result from the low solubility of Nb in cerianite (Kolodiazhnyi et al. 2016). In fergusonite, the crystal-field splitting parameter of tetrahedral Nb^{5+} is even lower ($10Dq_t$ is 4/9 of $10Dq_o$) explaining the small ΔE value of cubic Nb-substituted cerianite spectra.

Comparison of the splitting of Nb^{5+} XANES features with those of other $4d^0$ elements indicates an increase of the splitting with increasing cation charge. The splitting of Zr^{4+}, Nb^{5+} and Mo^{6+} coordinated to oxygen ligands in weakly distorted octahedra is 3.2 eV (Galoisy et al. 1999), 3.5–3.9 eV (this study) and 4.5 eV (Bare et al. 1993), respectively. This trend highlights the decrease of the ionic radius with increasing cation charge ($^{[6]}Zr^{4+}$ = 0.72 Å, $^{[6]}Nb^{5+}$ = 0.64 Å,

300 $^{[6]}Mo^{6+}$ = 0.59 Å, i.e. Shannon 1976) demonstrating the high sensitivity of $L_{2,3}$-edges XANES
301 spectroscopy to the speciation of $4d^0$ elements.

302 **Spectral broadening, charge transfer and site distortion.** Consideration of the C features
303 is required in the fitting procedure in order to avoid an overestimation of the broadening of the B
304 features. Unlike their assignment to $2p \rightarrow 5s$ transitions (Sugiura et al. 1988), our LFM calculations
305 show that this feature results from hybridization between the 4*d* orbitals of Nb^{5+} and the 2*p* orbitals
306 of O^{2-}, in agreement with the work of Okada and Kotani (1993) on Ti compounds.

307 Spectra of Nb-bearing minerals all display a high-energy shoulder of varying intensity at
308 2378 eV. The high degree of distortion of NbO_6 octahedra in columbite and niocalite (Table 1) is
309 not evidenced from the fit of their XANES spectra, which are characterized by B' shoulders of
310 limited intensity (Fig. 1). Furthermore, spectra of Nb perovskite and pyrochlore display the most
311 intense B' shoulder but these reference materials are composed of regular octahedra. The intensity
312 of the shoulder is therefore not related to the distortion of the NbO_6 octahedra. Spectra of niobian
313 perovksite, which exhibit the most intense C feature, is also the one with the largest B' shoulder.
314 We therefore ascribe the B' shoulder to orbital hybridization. The failure of ligand-field multiplet
315 calculations to reproduce both B' and C features (Fig. 5) may be due to the differences between the
316 Ti^{4+} charge-transfer parameters used here (Okada and Kotani 1993) and those of Nb^{5+}, which are
317 unknown.

318 The broadening of the XANES features for Ti^{4+} and Zr^{4+} (De Groot et al. 1992; Ikeno et al.
319 2013; Jollivet et al. 2013) indicates a distortion of the cation site. In contrast, the broadening of the
320 Nb $L_{2,3}$-XANES features, probed by the $FWHM_{B/A}$ parameter, is shaped by charge-transfer effects
321 and there is no correlation with the degree of distortion of the NbO_6 octahedra. The specifically
322 high contribution of charge-transfer effects to Nb $L_{2,3}$-XANES spectra is related to the covalent
323 character of the Nb–O bonds (Ikeno et al. 2011).

324 Spectra of Nb-substituted anatase and rutile display the poorest fit quality (χ^2 = 0.2–0.5) due
325 to poor fitting of the wide B features. The absence of a B' shoulder, suggesting the limited effect of

charge transfer on the spectra, reflects the distortion of the Nb sites (Fig. 2d). On the contrary, only the spectra of Nb-substituted hematite and goethite exhibit A and B features of similar widths, suggesting a symmetrical Nb site rather than the expected low symmetry of Fe^{3+} and the high distortion of FeO_6 octahedra. This hypothesis is supported by the good reproduction of the spectra of Nb-substituted hematite in O_h symmetry using LFM calculations. The similarities between the spectra of Nb-substituted hematite and goethite suggest similar Nb environments despite the different geometry of the Fe-octahedra in these minerals.

Spectral intensity variations and bond covalence. The intensity ratios (I_A/I_B) exhibit low standard deviations in our dataset ($\sigma = 0.13$ and 0.20 at the L_3 and L_2-edges, respectively). The low intensity ratio in the L_3-edge spectrum of Nb-substituted cerianite (0.75) stands out from the other references (1.10 on average for octahedral references). This can be explained by approximating the intensity ratio to the number of unoccupied states, i.e., 2/3 or 3/2 in regular cubic and octahedral coordination, respectively (Ogasawara et al. 2001). The intensity ratio values retrieved from the fitting procedure are not equal to the statistical values due to ligand-field multiplet effects (Ogasawara et al. 2001). However, the intensity ratio at the L_2-edge of the octahedral reference materials is close to the statistical value of 3/2 (1.46 on average) because this edge is less affected by multiplet effects (De Groot, 1994).

The intensity of the multiplet effects can be retrieved from our simulations through the reduction factor of the Slater-Condon integrals. The values of the reduction factor range from 0.35 to 0.54, indicating a major contribution from the covalent nature of the Nb-O bonds. These values are remarkably low compared to those around 0.7–0.8 observed in most oxides of 3*d* elements (De Groot 2005). However, the modeling of other Nb compounds, such as $CsNbF_6$, requires an even greater reduction of these parameters down to 40 % (De Groot et al. 1994). Therefore, the reduction of the Slater-Condon parameters mirrors the covalent nature of the bonds formed by 4*d* elements relative to 3*d* elements (Singh et al. 2017).

Why combine L_2 and L_3-edge XANES spectroscopy? As the spectral features are

correlated between the L_2 and L_3-edge (Supplemental Fig. S5), the in-depth analysis of only one edge is sufficient to determine the coordination number of Nb^{5+} and characterize the the local Nb environment. However, the simulation of XANES spectra using CFM and LFM calculations cannot be carried out on a single edge. The lower sensitivity of the L_2-edge to atomic-multiplets effects involves several pairs of solutions of the10*Dq* value and the reduction of Slater integrals that satisfactorily reproduce the L_2-edge spectra. Only the joint modeling of both edges constrains the reduction of the Slater integrals, because of their higher sensitivity to atomic-multiplet effects. The choice for the acquisition and analysis of one or combined edges depends on the precision of the crystallographic information one wants to extract from the spectra.

Mechanisms of Nb substitution in oxides

Niobium-substituted Ti oxides. The discrepancy between the average Ti–O distance in the host structure and the observed Nb–O distances points out specific mechanisms of substitution in Nb-substituted TiO_2 oxides (Fig. 6). Estimation of the Nb–O distances in Ti oxides by interpolation of the correlation between ΔE and R^{-5} gives values of ca. 2.03 Å for Nb-substituted anatase and ca. 2.01 Å and for Nb-substituted rutile. Such an increase of the Nb–O distances is expected from the larger ionic radius of Nb with respect to Ti ($^{[6]}Nb^{5+}$ = 0.64 Å and $^{[6]}Ti^{4+}$ = 0.605 Å, i.e. Shannon 1976). Moreover, the symmetry of the Nb^{5+} site in TiO_2 is reduced to a lower symmetrical group as evidenced by the broadening of the B_3 and B_2 features (Fig. 2d and Table 2). Increasing Nb substitution leads to lower ΔE and higher $FWHM_{B/A}$ (Table 2), indicating an increased distortion of the Nb sites and increased Nb–O distances. Such distortion of Nb sites and an increase in Nb–O distances with increasing amounts of Nb were also evidenced using EXAFS (1.98 Å and 1.99 Å for $Ti_{0.97}Nb_{0.03}O_2$ and $Ti_{0.92}Nb_{0.08}O_2$, respectively, i.e. Gardecka et al. 2015). The mechanism allowing the incorporation of Nb^{5+} in rutile and anatase is the formation of one Ti^{4+} vacancy for every four Nb^{5+} (Sheppard et al. 2006) following conditions of equilibrium and electroneutrality (Sheppard 2007) as illustrated by the Kröger-Vink notation:

$$2[Nb_2O_5] \Leftrightarrow 4[Nb_{Ti}^{\bullet}] + [V_{Ti}''''] + 10[O_O^x] \quad (1)$$

$$4[V_{Ti}''''] = [Nb_{Ti}^{\bullet}] \quad (2)$$

In geological environments, the substitution of Nb^{5+} for Ti^{4+} in Ti oxides is also expected to be accommodated by interstitial Fe^{3+} in oxidized environments following the substitution $2Ti^{4+} = Fe^{3+} + 2Nb^{5+}$ (Ruck et al. 1986) and by Fe^{2+} in reducing environments, according to $3Ti^{4+} = Fe^{2+} + 2Nb^{5+}$ (Giovannini et al. 2020).

Recent EXAFS analyses have highlighted the splitting of the first shell into two Nb-O contributions at 1.88 and 2.01 Å in Nb-substituted anatase (Ribeiro et al. 2020). The increase of Nb–O distances up to ca. 2.01 Å in the latter study and this work could reflect the presence of Nb_2O_5 clusters in Nb-substituted anatase and rutile (Atanacio et al. 2014), as the values of Nb–O distances in Nb_2O_5 are also 2.01 Å (Table 1). Even if the formation of Nb_2O_5 clusters cannot be excluded, the differences between the spectra of Nb_2O_5 and Nb-substituted TiO_2 (Table 2) indicate that Nb clustering is not an important process.

Niobium-substituted Fe oxides. In hematite and goethite, Fe^{3+} has a similar ionic radius ($^{[6]}Fe^{3+}$ = 0.645 Å, i.e. Shannon 1976) to Nb^{5+} ($^{[6]}Nb^{5+}$ = 0.64 Å). The substitution of Nb^{5+} for Fe^{3+} in goethite has been shown to be isomorphic (Oliveira et al. 2008). Despite the difference between the Fe sites in hematite and goethite (Table 1), the similar Nb XANES spectra also argue for an isomorphic substitution in hematite. Charge balance may be maintained by substituting $5Fe^{3+}$ for $3Nb^{5+}$, which induces cation vacancies. Our study shows that Nb-substituted Fe oxides can be reproduced by CFM and LFM calculations in a regular O_h site symmetry even though the initial Fe site has a C_3 symmetry (Figs. 3b and 4b). The regularity of the NbO_6 octahedra is also supported by the absence of broadening of features B_3 and B_2 (Fig. 2c). The alignment of their experimental ΔE values on the trend with respect to theoretical Fe–O distances (Fig. 6) indicates that the average Nb–O distances are not significantly modified with respect to the average Fe–O distances.

However, EXAFS data on Nb-substituted hematite indicate low values of Nb–O distances

(1.87 and 2.05 Å) compared to the Fe–O distances in hematite (1.92 and 2.11 Å, i.e. Silva et al. 2009). The differences between our results and those of Silva et al. (2009) could reflect the high amounts of Nb incorporated in the Fe oxides (5 and 10 wt% Nb) or the synthesis protocol. The incorporation of Nb in Fe oxides may result in a symmetrization of the Nb site due to the relaxation of the crystal structure around Nb arising from the induced cation vacancies.

Niobium-substituted cerianite. Charge and size differences (0.97 and 0.64 Å, for Ce^{4+} and Nb^{5+} respectively, i.e. Shannon 1976) limit the substitution of Nb in cerianite. The substitution of Nb^{5+} for Ce^{4+} was explained by the displacement of Nb^{5+} cations from ideal cubic symmetry that leads to oxygen vacancies (Hiley et al. 2018). It has also been suggested that half of the Ce ions become trivalent to account for charge balance. The other half of the charge compensation would be accommodated by interstitial oxygens (Kolodiazhnyi et al. 2016) according to:

$$[Nb_{Ce}^{\bullet}] = [Ce_{Ce}'] + 2[O_i''] + [O_i']$$

Our simulation of the Nb-substituted spectrum in O_h point symmetry (Fig. 3a) indicates that a Nb^{5+}–Nd^{3+} co-doping eases the charge balance equilibrium ($2[Ce^{4+}] = [Nb^{5+}] + [Nd^{3+}]$) and prevents significant distortion of the Nb site by limiting the formation of interstitial oxygen and vacancies.

IMPLICATIONS

Deciphering the origin of the properties of technological Nb-substituted oxides

The synthetic Nb-bearing oxides selected in this study are considered important in meeting technological challenges associated with climate change mitigation or environmental decontamination (e.g., Ismael 2020; Ma et al. 2020). Among other applications, they are used for dye-sensitized solar cells (Lü et al. 2010), Na-ion battery anodes (Usui et al. 2015), direct solar fuel conversion (Fu et al. 2016) and catalysts for the removal of exhaust-gas nitrogen oxide (Lian et al. 2015). These enhanced physico-chemical properties result from the substitution of Nb^{5+} for a cation, leading to oxide mobility and transport properties due to charge unbalancing, oxygen vacancies or

interstitials. The properties of these Nb materials may be rationalized through a knowledge of the mechanisms of Nb insertion, which can be unveiled by Nb $L_{2,3}$-edges XANES spectroscopy.

Upgrading ore processing through quantitative analysis of Nb speciation

The choice of Nb ore-processing strategies depends on the nature of the Nb minerals, their degree of alteration and their crystal-chemical variability. It is essential to correctly characterize the Nb ores to optimize ore processing (Černý and Ercit 1989). Niobium recovery from pyrochlore using amine collectors is currently being used in the three ore processing plants worldwide (Guimaraes and Weiss 2001). Nevertheless, this process induces a significant loss of columbite and Nb-rutile between feed and concentrate (Gibson et al. 2015). Moreover, high concentration of Fe in pyrochlore, which is a typical feature of hydropyrochlore, reduces its floatability and causes Nb loss during ore processing (Chehreh Chelgani et al. 2012). Niobian rutile has also been identified in the world-class deposit of Araxá but its significance in the overall Nb budget remains elusive (Neumann and Medeiros 2015). Niobium XANES spectroscopy is a useful tool to identify Nb speciation in ore minerals to optimize ore-processing strategies.

Unravelling Nb geochemical behavior in natural systems

Recent findings in hydrothermal contexts (Andersson et al. 2018; Dietzel et al. 2019) and near-surface conditions (Wall et al. 1996; Chakrabarty et al. 2013; Giovannini et al. 2017) demonstrate the alteration of Nb minerals and question the presumed immobility of Nb (MacLean and Barrett 1993). The demonstrated sensitivity of Nb $L_{2,3}$-edges XANES spectroscopy opens up the possibility to track Nb mineral speciation in weathered Nb-enriched samples. It can also be used to determine the mechanisms of alteration of primary Nb minerals and reveal the mechanisms of Nb incorporation in newly-formed phases. A combination of bulk and micro-XANES analyses can thus be used to enlighten the molecular-scale and geochemical factors that induce contrasted Nb dynamics in supergene environments as has been done for rare-earth elements (Janots et al. 2015; Chassé et al. 2019; Borst et al. 2020).

ACKNOWLEDGMENTS

We are grateful to Jean-Claude Boulliard and Éloïse Gaillou for the supply of rare mineral species from the Sorbonne Université and École Nationale Supérieure des Mines de Paris mineralogy (MINES ParisTech) collections. Alain Demourgues and Guillaume Gouget are thanked for providing the niobate samples and commenting the manuscript. We thank Sophie Cassaignon and Tsou Hsi Camille Chan Chang for the synthesis of Nb-substituted anatase. We thank Benoît Baptiste, Ludovic Delbes, Michel Fialin and Nicolas Rividi for experimental support during XRD and EPMA analyses. We acknowledge SOLEIL for provision of synchrotron radiation facilities and thank the staff of the LUCIA beamline for their help in the measurement of Nb $L_{2,3}$-edges (Proposal No. 20191239).

REFERENCES

Andersson, S. (1967) The crystal structure of N-Nb_2O_5, prepared in the presence of small amounts of LiF. Zeitschrift für anorganische und allgemeine Chemie, 351, 106–112.

Andersson, S.S., Wagner, T., Jonsson, E., and Michallik, R.M. (2018) Mineralogy, paragenesis, and mineral chemistry of REEs in the Olserum-Djupedal REE-phosphate mineralization, SE Sweden. American Mineralogist, 103, 125–142.

Atanacio, A.J., Bak, T., and Nowotny, J. (2014) Niobium segregation in niobium-doped titanium dioxide (rutile). The Journal of Physical Chemistry C, 118, 11174–11185.

Bare, S.R., Mitchell, J.G.E., Maj, J.J., and Glands, J.L. (1993) Local site symmetry of dispersed molybdenum oxide catalysts: XANES at the Mo $L_{2,3}$-edges. The Journal of Physical Chemistry, 97, 6048–6053.

Bhattacharyya, A., Schmidt, M.P., Stavitski, E., Azimzadeh, B., and Martínez, C.E. (2019) Ligands representing important functional groups of natural organic matter facilitate Fe redox transformations and resulting binding environments. Geochimica et Cosmochimica Acta, 251, 157–175.

Borst, A.M., Smith, M.P., Finch, A.A., Estrade, G., Villanova-de-Benavent, C., Nason, P., Marquis, E., Horsburgh, N.J., Goodenough, K.M., Xu, C., and others (2020) Adsorption of rare earth elements in regolith-hosted clay deposits. Nature Communications, 11, 4386.

Bourdelle, F., Benzerara, K., Beyssac, O., Cosmidis, J., Neuville, D.R., Brown, G.E., and Paineau, E. (2013) Quantification of the ferric/ferrous iron ratio in silicates by scanning transmission X-ray microscopy at the Fe $L_{2,3}$edges. Contributions to Mineralogy and Petrology, 166, 423–434.

Brotton, S.J., Shapiro, R., van der Laan, G., Guo, J., Glans, P.-A., and Ajello, J.M. (2007) Valence state fossils in Proterozoic stromatolites by L-edge X-ray absorption spectroscopy. Journal of Geophysical Research: Biogeosciences, 112.

Burns, R.G. (1993) Mineralogical applications of crystal field theory, 2nd ed. Cambridge University Press.

Cartier, C., Hammouda, T., Boyet, M., Mathon, O., Testemale, D., and Moine, B.N. (2015) Evidence for Nb^{2+} and Ta^{3+} in silicate melts under highly reducing conditions: A XANES study. American Mineralogist, 100, 2152–2158.

Černý, P., and Ercit, T.S. (1989) Mineralogy of niobium and tantalum: Crystal chemical relationships, paragenetic aspects and their economic implications. In P. Möller, Petr Černý, and F.

Saupé, Eds., Lanthanides, Tantalum and Niobium pp. 27–79. Springer Berlin Heidelberg, Berlin, Heidelberg.

Chakrabarty, A., Mitchell, R.H., Ren, M., Sen, A.K., and Pruseth, K.L. (2013) Rinkite, cerianite-(Ce), and hingganite-(Ce) in syenite gneisses from the Sushina Hill Complex, India: Occurrence, compositional data and petrogenetic significance. Mineralogical Magazine, 77, 3137–3153.

Chassé, M., Griffin, W.L., O'Reilly, S.Y., and Calas, G. (2017) Scandium speciation in a world-class lateritic deposit. Geochemical Perspectives Letters, 3, 105–114.

Chassé, M., Griffin, W.L., O'Reilly, S.Y., and Calas, G. (2019) Australian laterites reveal mechanisms governing scandium dynamics in the critical zone. Geochimica et Cosmochimica Acta, 260, 292–310.

Chehreh Chelgani, S., Hart, B., Marois, J., and Ourriban, M. (2012) Study of pyrochlore matrix composition effects on froth flotation by SEM–EDX. Minerals Engineering, 30, 62–66.

De Groot, F.M.F (2005) Multiplet effects in X-ray spectroscopy. Coordination Chemistry Reviews, 249, 31–63.

De Groot, F.M.F, Figueiredo, M.O., Basto, M.J., Abbate, M., Petersen, H. and Fuggle, J.C. (1992) 2*p* X-ray absorption of titanium in minerals. Physics and Chemistry of Minerals, 19, 140–147.

De Groot, F.M.F., Hu, Z.W., Lopez, M.F., Kaindl, G., Guillot, F., and Tronc, M. (1994) Differences between L_3 and L_2 X-ray absorption spectra of transition metal compounds. The Journal of Chemical Physics, 101, 6570–6576.

Dietzel, C.A.F., Kristandt, T., Dahlgren, S., Giebel, R.J., Marks, M.A.W., Wenzel, T., and Markl, G. (2019) Hydrothermal processes in the Fen alkaline-carbonatite complex, southern Norway. Ore Geology Reviews, 111, 102969.

Dufour, F., Cassaignon, S., Durupthy, O., Colbeau-Justin, C., and Chanéac, C. (2012) Do TiO_2 nanoparticles really taste better when cooked in a microwave oven? European Journal of Inorganic Chemistry, 2012, 2707–2715.

European Commission (2020) Study on the EU's list of critical raw materials - Final Report.

Ewing, R.C. (1975) The crystal chemistry of complex niobium and tantalum oxides. IV. The metamict state: Discussion. American Mineralogist, 60, 728–733.

Friis, H., and Casey, W.H. (2018) Niobium Is highly mobile as a polyoxometalate ion during natural weathering. The Canadian Mineralogist, 56, 905–912.

Fu, Y., Dong, C.-L., Lee, W.-Y., Chen, J., Guo, P., Zhao, L., and Shen, S. (2016) Nb-doped hematite nanorods for efficient solar water splitting: Electronic structure evolution versus morphology alteration. ChemNanoMat, 2, 704–711.

Galoisy, L., Pélegrin, E., Arrio, M.-A., Ildefonse, P., Calas, G., Ghaleb, D., Fillet, C., and Pacaud, F. (1999) Evidence for 6-coordinated zirconium in inactive nuclear waste glasses. Journal of the American Ceramic Society, 82, 2219–2224.

Gardecka, A.J., Goh, G.K.L., Sankar, G., and Parkin, I.P. (2015) On the nature of niobium substitution in niobium doped titania thin films by AACVD and its impact on electrical and optical properties. Journal of Materials Chemistry A, 3, 17755–17762.

Gibson, C., Aghamirian, M., and Kelebek, S. (2015) Challenges in Niobium Flotation, 11.

Giovannini, A.L., Bastos Neto, A.C., Porto, C.G., Pereira, V.P., Takehara, L., Barbanson, L., and Bastos, P.H.S. (2017) Mineralogy and geochemistry of laterites from the Morro dos Seis Lagos Nb (Ti, REE) deposit (Amazonas, Brazil). Ore Geology Reviews, 88, 461–480.

Giovannini, A.L., Mitchell, R.H., Bastos Neto, A.C., Moura, C.A.V., Pereira, V.P., and Porto, C.G. (2020) Mineralogy and geochemistry of the Morro dos Seis Lagos siderite carbonatite, Amazonas, Brazil. Lithos, 360–361, 105433.

Gouget, G., Duttine, M., Chung, U.-C., Fourcade, S., Mauvy, F., Braida, M.-D., Le Mercier, T., and Demourgues, A. (2019) High ionic conductivity in oxygen-deficient Ti-substituted sodium niobates and the key role of structural features. Chemistry of Materials, 31, 2828–2841.

Guimaraes, H.N., and Weiss, R.A. (2001) The complexity of the niobium deposits in the alkaline-ultramafic intrusions Catalao I and II - Brazil. Mineralcao Catalao.

Haverkort, M.W. (2016) *Quanty* for core level spectroscopy - excitons, resonances and band excitations in time and frequency domain. Journal of Physics: Conference Series, 712, 012001.

Haverkort, M.W., Zwierzycki, M., and Andersen, O.K. (2012) Multiplet ligand-field theory using Wannier orbitals. Physical Review B, 85, 165113.

Henderson, G.S., de Groot, F.M.F., and Moulton, B.J.A. (2014) X-ray Absorption Near-Edge Structure (XANES) Spectroscopy. Reviews in Mineralogy and Geochemistry, 78, 75–138.

Hiley, C.I., Playford, H.Y., Fisher, J.M., Felix, N.C., Thompsett, D., Kashtiban, R.J., and Walton, R.I. (2018) Pair distribution function analysis of structural disorder by Nb^{5+} inclusion in ceria: Evidence for enhanced oxygen storage capacity from under-coordinated oxide. Journal of the American Chemical Society, 140, 1588–1591.

Hill, I.G., Worden, R.H., and Meighan, I.G. (2000) Geochemical evolution of a palaeolaterite: the Interbasaltic Formation, Northern Ireland. Chemical Geology, 166, 65–84.

Höche, T., Ikeno, H., Mader, M., Henderson, G.S., Blyth, R.I.R., Sales, B.C., and Tanaka, I. (2013) Vanadium $L_{2,3}$ XANES experiments and first-principles multielectron calculations: Impact of

second-nearest neighboring cations on vanadium-bearing fresnoites. American Mineralogist, 98, 665–670.

Ikeno, H., Mizoguchi, T. and Tanaka, I. (2011) *Ab initio* charge transfer multiplet calculations on the $L_{2,3}$ XANES and ELNES of *3d* transition metal oxides. Physical Review B, 83, 155107.

Ikeno, H., Krause, M., Höche, T., Patzig, C., Hu, Y., Gawronski, A., Tanaka, I. and Rüssel, C. (2013) Variation of Zr-$L_{2,3}$ XANES in tetravalent zirconium oxides. Journal of Physics: Condensed Matter, 25. 165505.

Ismael, M. (2020) A review and recent advances in solar-to-hydrogen energy conversion based on photocatalytic water splitting over doped-TiO_2 nanoparticles. Solar Energy, 211, 522–546.

Janots, E., Bernier, F., Brunet, F., Muñoz, M., Trcera, N., Berger, A., and Lanson, M. (2015) Ce(III) and Ce(IV) (re)distribution and fractionation in a laterite profile from Madagascar: Insights from in situ XANES spectroscopy at the Ce L_{III}-edge. Geochimica et Cosmochimica Acta, 153, 134–148.

Jollivet, P., Calas, G., Galoisy, L., Angeli, F., Bergeron, B., Gin, S., Ruffoni, M.P., and Trcera, N. (2013) An enhanced resolution of the structural environment of zirconium in borosilicate glasses. Journal of Non-Crystalline Solids, 381, 40–47.

Kalfoun, F., Ionov, D., and Merlet, C. (2002) HFSE residence and Nb/Ta ratios in metasomatised, rutile-bearing mantle peridotites. Earth and Planetary Science Letters, 199, 49–65.

Kolodiazhnyi, T., Sakurai, H., Belik, A.A., and Gornostaeva, O.V. (2016) Unusual lattice evolution and magnetochemistry of Nb doped CeO_2. Acta Materialia, 113, 116–123.

Krause, M.O., and Oliver, J.H. (1979) Natural widths of atomic *K* and *L* levels, *Kα* X-ray lines and several *KLL* Auger lines. Journal of Physical and Chemical Reference Data, 8, 329–338.

Kubouchi, Y., Hayakawa, S., Namatame, H., and Hirokawa, T. (2012) Direct observation of fractional change of niobium ionic species in a solution by means of X-ray absorption fine structure spectroscopy: XAFS spectroscopy of solutions. X-Ray Spectrometry, 41, 259–263.

Kunz, M., and Brown, I.D. (1995) Out-of-center distortions around octahedrally coordinated d^0 transition metals. Journal of Solid State Chemistry, 115, 395–406.

Kurtz, A.C., Derry, L.A., Chadwick, O.A., and Alfano, M.J. (2000) Refractory element mobility in volcanic soils. Geology, 28, 683–686.

Lee, M.J., Lee, J.I., Garcia, D., Moutte, J., Williams, C.T., Wall, F., and Kim, Y. (2006) Pyrochlore chemistry from the Sokli phoscorite-carbonatite complex, Finland: Implications for the genesis of phoscorite and carbonatite association. Geochemical Journal, 40, 1–13.

Lian, Z., Liu, F., He, H., and Liu, K. (2015) Nb-doped VO_x/CeO_2 catalyst for NH_3-SCR of NO_x at low temperatures. RSC Advances, 5, 37675–37681.

Linnen, R.L., and Cuney, M. (2005) Granite-Related Rare-Element Deposits and Experimental Constraints on Ta-Nb-W-Sn-Zr-Hf Mineralization, 45–68.

Lottermoser, B.G., and England, B.M. (1988) Compositional variation in pyrochlores from the Mt Weld carbonatite laterite, Western Australia. Mineralogy and Petrology, 38, 37–51.

Lü, X., Mou, X., Wu, J., Zhang, D., Zhang, L., Huang, F., Xu, F., and Huang, S. (2010) Improved-performance dye-sensitized solar cells using Nb-doped TiO_2 electrodes: Efficient electron injection and transfer. Advanced Functional Materials, 20, 509–515.

Ma, J., Guo, X., Xue, H., Pan, K., Liu, C., and Pang, H. (2020) Niobium/tantalum-based materials: Synthesis and applications in electrochemical energy storage. Chemical Engineering Journal, 380, 122428.

MacLean, W.H., and Barrett, T.J. (1993) Lithogeochemical techniques using immobile elements. Journal of Geochemical Exploration, 48, 109–133.

Mitchell, R.H. (2015) Primary and secondary niobium mineral deposits associated with carbonatites. Ore Geology Reviews, 64, 626–641.

Nabi, M.M., Wang, J., Meyer, M., Croteau, M.-N., Ismail, N., and Baalousha, M. (2021) Concentrations and size distribution of TiO_2 and Ag engineered particles in five wastewater treatment plants in the United States. Science of The Total Environment, 753, 142017.

Neumann, R., and Medeiros, E.B. (2015) Comprehensive mineralogical and technological characterisation of the Araxá (SE Brazil) complex REE (Nb-P) ore, and the fate of its processing. International Journal of Mineral Processing, 144, 1–10.

Newville, M. (2013) Larch: An analysis package for XAFS and related spectroscopies. Journal of Physics: Conference Series, 430, 012007.

Ogasawara, K., Iwata, T., Koyama, Y., Ishii, T., Tanaka, I., and Adachi, H. (2001) Relativistic cluster calculation of ligand-field multiplet effects on cation $L_{2,3}$ *X*-ray-absorption edges of $SrTiO_3$, NiO, and CaF_2. Physical Review B, 64, 115413.

Okada, K., and Kotani, A. (1993) Theory of core level X-ray photoemission and photoabsorption in Ti compounds. Journal of Electron Spectroscopy and Related Phenomena, 62, 131–140.

Olegário, R.C., Ferreira de Souza, E.C., Marcelino Borges, J.F., Marimon da Cunha, J.B., Chaves de Andrade, A.V., Masetto Antunes, S.R., and Antunes, A.C. (2013) Synthesis and characterization of Fe^{3+} doped cerium–praseodymium oxide pigments. Dyes and Pigments, 97, 113–117.

Oliveira, L.C.A., Ramalho, T.C., Souza, E.F., Gonçalves, M., Oliveira, D.Q.L., Pereira, M.C., and Fabris, J.D. (2008) Catalytic properties of goethite prepared in the presence of Nb on oxidation

reactions in water: Computational and experimental studies. Applied Catalysis B: Environmental, 83, 169–176.

Piilonen, P.C., Farges, F., Linnen, R.L., Brown, G.E., Pawlak, M., and Pratt, A. (2006) Structural environment of Nb^{5+} in dry and fluid-rich (H_2O,F) silicate glasses: A combined XANES and EXAFS study. The Canadian Mineralogist, 44, 775–794.

Retegan, M. (2019) Crispy: v0.7.3.

Ribeiro, J.M., Correia, F.C., Kuzmin, A., Jonane, I., Kong, M., Goñi, A.R., Reparaz, J.S., Kalinko, A., Welter, E., and Tavares, C.J. (2020) Influence of Nb-doping on the local structure and thermoelectric properties of transparent TiO_2:Nb thin films. Journal of Alloys and Compounds, 838, 155561.

Ruck, R., Babkine, J., Nguyen, C., Marnier, G., and Dusausoy, Y. (1986) Geochemical association of Fe and Nb in synthetic and natural cassiterites and rutiles. In Experimental Mineralogy and Geochemistry pp. 122–123. Nancy.

Rudnick, R.L., and Gao, S. (2014) Composition of the Continental Crust. In Treatise on Geochemistry pp. 1–51. Elsevier.

Schaefers, F., Mertin, M., and Gorgoi, M. (2007) KMC-1: A high resolution and high flux soft X-ray beamline at BESSY. Review of Scientific Instruments, 78, 123102.

Schulz, K.J., Piatak, N.M., and Papp, J.F. (2017) Niobium and Tantalum p. 34. Professional Paper, USGS, Reston, Virginia.

Shannon, R.D. (1976) Revised effective ionic radii and systematic studies of interatomic distances in halides and chaleogenides. Acta Crystallographica Section B Structural Crystallography and Crystal Chemistry, A32, 751–767.

Sheppard, L., Bak, T., Nowotny, J., Sorrell, C.C., Kumar, S., Gerson, A.R., Barnes, M.C., and Ball, C. (2006) Effect of niobium on the structure of titanium dioxide thin films. Thin Solid Films, 510, 119–124.

Sheppard, L.R. (2007) Defect chemistry and charge transport in niobium-doped titanium dioxide. University of New South Wales, Australia.

Silva, A.C., Oliveira, D.Q.L., Oliveira, L.C.A., Anastácio, A.S., Ramalho, T.C., Lopes, J.H., Carvalho, H.W.P., and Torres, C.E.R. (2009) Nb-containing hematites $Fe_{2-x}Nb_xO_3$: The role of Nb^{5+} on the reactivity in presence of the H_2O_2 or ultraviolet light. Applied Catalysis A: General, 357, 79–84.

Singh, S.K., Eng, J., Atanasov, M., and Neese, F. (2017) Covalency and chemical bonding in transition metal complexes: An ab initio based ligand field perspective. Coordination Chemistry Reviews, 344, 2–25.

Sugiura, C., Kitamura, M., and Mijramatsu, S. (1988) Niobium L_{III} and L_{II} X-ray absorption-edge spectra of Nb_2O_5 and NH_4NbF_6. Journal of Physics and Chemistry of Solids, 49, 1095–1099.

Usui, H., Yoshioka, S., Wasada, K., Shimizu, M., and Sakaguchi, H. (2015) Nb-doped rutile TiO_2: A potential anode material for Na-ion battery. ACS Applied Materials & Interfaces, 7, 6567–6573.

Vantelon, D., Trcera, N., Roy, D., Moreno, T., Mailly, D., Guilet, S., Metchalkov, E., Delmotte, F., Lassalle, B., Lagarde, P., and others (2016) The LUCIA beamline at SOLEIL. Journal of Synchrotron Radiation, 23, 635–640.

Vercamer, V., Hunault, M.O.J.Y., Lelong, G., Haverkort, M.W., Calas, G., Arai, Y., Hijiya, H., Paulatto, L., Brouder, C., Arrio, M.-A., and others (2016) Calculation of optical and K pre-edge absorption spectra for ferrous iron of distorted sites in oxide crystals. Physical Review B, 94, 245115.

Wall, F., Williams, C.T., Woolley, A.R., and Nasraoui, M. (1996) Pyrochlore from weathered carbonatite at Lueshe, Zaire. Mineralogical Magazine, 60, 731–750.

Walter, B.F., Parsapoor, A., Braunger, S., Marks, M.A.W., Wenzel, T., Martin, M., and Markl, G. (2018) Pyrochlore as a monitor for magmatic and hydrothermal processes in carbonatites from the Kaiserstuhl volcanic complex (SW Germany). Chemical Geology, 498, 1–16.

Wang, B., Zhao, Y., Banis, M.N., Sun, Q., Adair, K.R., Li, R., Sham, T.-K., and Sun, X. (2018) Atomic layer deposition of lithium niobium oxides as potential solid-state electrolytes for lithium-ion batteries. ACS Applied Materials & Interfaces, 10, 1654–1661.

Waring, J.L., Roth, R.S., and Parker, H.S. (1973) Temperature-pressure phase relationships in niobium pentoxide. Journal of Research of the National Bureau of Standards Section A: Physics and Chemistry, 77A, 705.

Waroquiers, D., Gonze, X., Rignanese, G.-M., Welker-Nieuwoudt, C., Rosowski, F., Goebel, M., Schenk, S., Degelmann, P., Andre, R., Glaum, R., and others (2017) Statistical analysis of coordination environments in oxides. Chemistry of Materials, 29, 8346–8360.

Weng, T.-C., Waldo, G.S., and Penner-Hahn, J.E. (2005) A method for normalization of X-ray absorption spectra. Journal of Synchrotron Radiation, 12, 506–510.

Wu, B., Hu, Y.-Q., Bonnetti, C., Xu, C., Wang, R.-C., Zhang, Z.-S., Li, Z.-Y., and Yin, R. (2021) Hydrothermal alteration of pyrochlore group minerals from the Miaoya carbonatite complex, central China and its implications for Nb mineralization. Ore Geology Reviews, 132, 104059.

Yashiro, K. (2004) Electrical properties and defect structure of niobia-doped ceria. Solid State Ionics, 175, 341–344.

Zietlow, P., Beirau, T., Mihailova, B., Groat, L.A., Chudy, T., Shelyug, A., Navrotsky, A., Ewing, R.C., Schlüter, J., Škoda, R., and others (2017) Thermal annealing of natural, radiation-damaged pyrochlore. Zeitschrift für Kristallographie - Crystalline Materials, 232.

Minerals (group *i,ii,iii*)	Ideal formula	Structure	Coordination number	Nb site symmetry	Average cation–O distances (Å)	Distortion index (%)	Location
Natural samples							
(i) Fluorcalciopyrochlore	$(Ca,Na)_2(Nb,Ti)_2O_6F$	Corner-sharing NbO_6 octahedra sharing edges with A site cation	6	D_{3d}	1.944	0.0	Tatarka. Russia (SU)
(i) Hydropyrochlore	$(H_2O,□□)Nb_2(O.OH)_6(H_2O)$	Corner-sharing NbO_6 octahedra sharing edges with A site cation	6	D_{3d}	1.972	0.0	Lueshe. Congo (SU)
(i) Columbite-(Mn)	$(Mn,Fe)(Nb,Ta)_2O_6$	Chains of edge-sharing NbO_6 octahedra	6	C_1	2.017	6.0	Musha. Rwanda (ENSMP)
(ii) Niobian perovskite	$CaTi_{1-2x}Fe_xNb_xO_3$	Perovskite structure (ABO_3) with interconnected NbO_6 octahedra with interstitial Ca	6	C_1	1.966	0.6	Oka. Canada (ENSMP)
(ii) Niocalite	$Ca_7Nb(Si_4O_{14})O_3F$	Isolated NbO_6 octahedra sharing edges and corners with CaO_6 octahedra	6	C_1	2.049	6.1	Oka. Canada (ENSMP)
Synthetic samples							
(ii) Lueshite	$NaNbO_3$	Perovskite structure (ABO_3) with interconnected NbO_6 octahedra with interstitial Na	6	C_1	1.990	2.8	
(iii) Rutile (5 wt% Nb)	TiO_2	Edge and corner-sharing TiO_6 octahedra (2 edges are shared with each other)	6	D_{2h}	1.956	0.6	
(iii) Anatase (5 wt% Nb)	TiO_2	Edge-sharing TiO_6 octahedra (4 edges are shared with each other)	6	D_{2d}	1.949	1.0	
(iii) Hematite (1 wt% Nb)	α-Fe_2O_3	Face and edge-sharing FeO_6 octahedra	6	C_3	2.031	4.2	
(iii) Goethite (1 wt% Nb)	α-FeOOH	Chains of edge-sharing FeO_6 octahedra joined by corner-sharing FeO_6	6	C_s	2.026	3.8	
(iii) Cerianite (1 wt% Nb)	CeO_2	Edge-sharing CeO_8 cubes	8	O_h	2.343	0.0	
Nb_2O_5	Nb_2O_5	Edge and corner-sharing NbO_6 octahedra. 1 out of 28 Nb sites is a tetrahedron	6	C_1	2.014	1.5	

	L_3-edge				L_2-edge			
Samples	**ΔE (eV)**	**I_A/I_B**	**$FWHM_{B/A}$**	**χ^2**	**ΔE (eV)**	**I_A/I_B**	**$FWHM_{B/A}$**	**χ^2**
Nb cerianite	2.55	0.75	1.47	0.06	2.29	0.96	1.73	0.06
Nb_2O_5	3.28	0.94	1.73	0.04	3.06	1.24	1.92	0.04
Fluorcalciopyrochlore	3.90	1.18	1.48	0.09	3.83	1.55	1.69	0.06
Hydropyrochlore	3.76	1.07	1.62	0.05	3.64	1.41	1.67	0.04
Columbite	3.41	1.11	1.48	0.06	3.32	1.47	1.73	0.06
Niocalite	3.43	1.17	1.38	0.11	3.44	1.55	1.63	0.10
Lueshite	3.54	1.05	1.68	0.08	3.75	1.42	1.28	0.09
Nb perovskite	3.96	1.20	2.08	0.39	3.95	1.60	2.35	0.16
Nb hematite	3.44	1.08	1.12	0.28	3.47	1.45	1.39	0.10
Nb goethite	3.46	1.08	1.18	0.25	3.48	1.46	1.47	0.11
Nb anatase 1% Nb	3.38	1.10	1.58	0.51	3.30	1.48	1.84	0.19
Nb anatase 5% Nb	3.34	1.14	1.62	0.41	3.29	1.55	1.88	0.17
Nb anatase 10% Nb	3.33	1.14	1.61	0.39	3.28	1.55	1.92	0.15
Nb rutile 5% Nb	3.45	1.03	1.54	0.21	3.31	1.25	1.78	0.09

CFM parameters	Nb point group symmetry	Slater integrals reduction	10*Dq*	*Ds*	*Dt*
Nb-substituted cerianite	O_h	0.51	2.80	/	/
Nb-substituted hematite	O_h	0.51	3.70	/	/
Hydropyrochlore	O_h	0.54	3.90	/	/
Latrappite	D_{4h}	0.50	6.70	0.40	0.24

Sample	Nb point group symmetry	Slater integrals reduction	$10Dq$ (eV)	U_{dd} (eV)	U_{dc} (eV)	Δ (eV)	$V_{e\,g}$ (eV)	$V_{t\,2g}$ (eV)
Nb-substituted hematite	O_h	0.70	2.25	2.0	6.0	4.0	4.0	-2.0

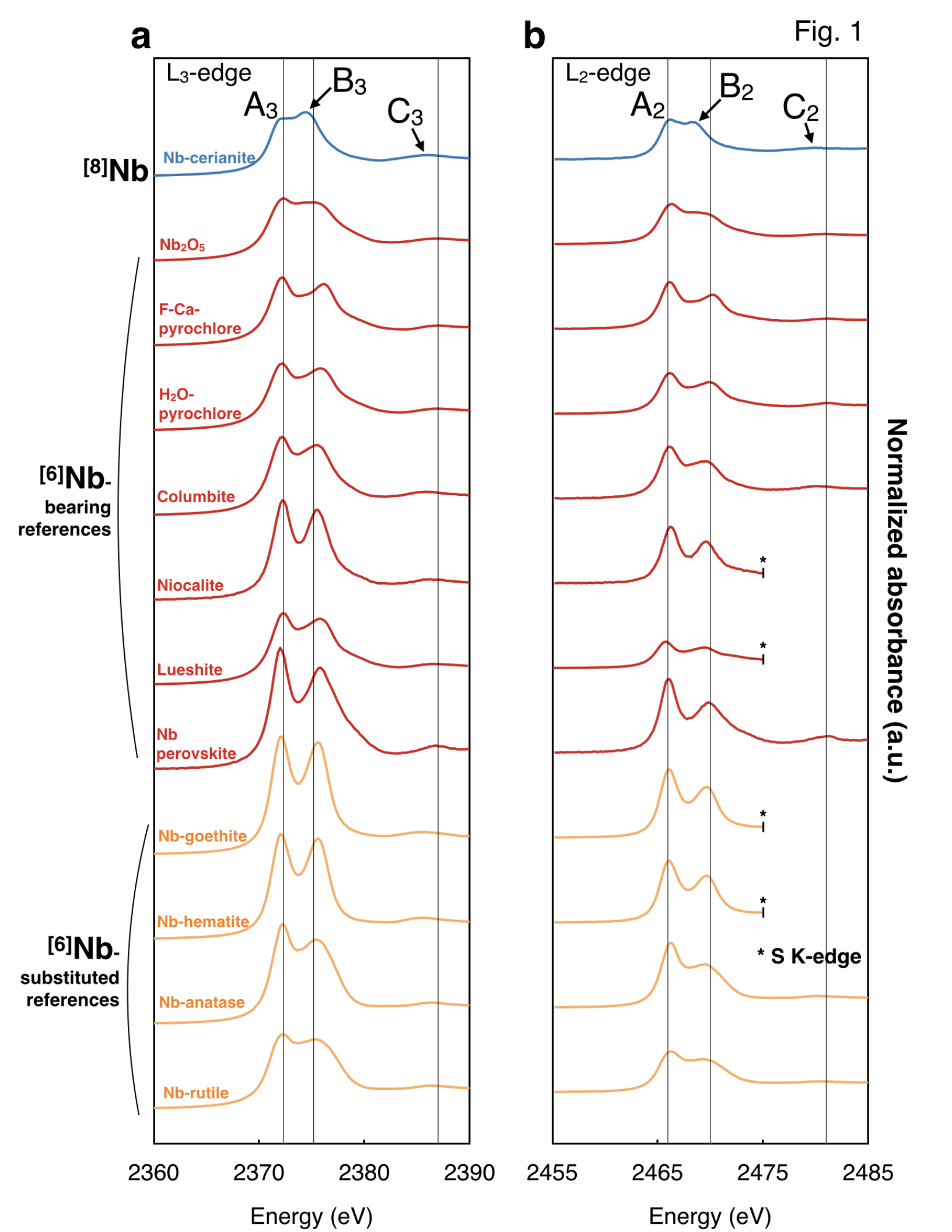
a
b
Fig. 1
L3-edge
A3
B3
C3
L2-edge
A2
B2
C2
[8]Nb
Nb-cerianite
Nb2O5
F-Ca-pyrochlore
H2O-pyrochlore
Columbite
Niocalite
Lueshite
Nb perovskite
[6]Nb-bearing references
Nb-goethite
Nb-hematite
Nb-anatase
Nb-rutile
[6]Nb-substituted references
* S K-edge
Normalized absorbance (a.u.)
2360
2370
2380
2390
2455
2465
2475
2485
Energy (eV)
Energy (eV)

Fig. 2

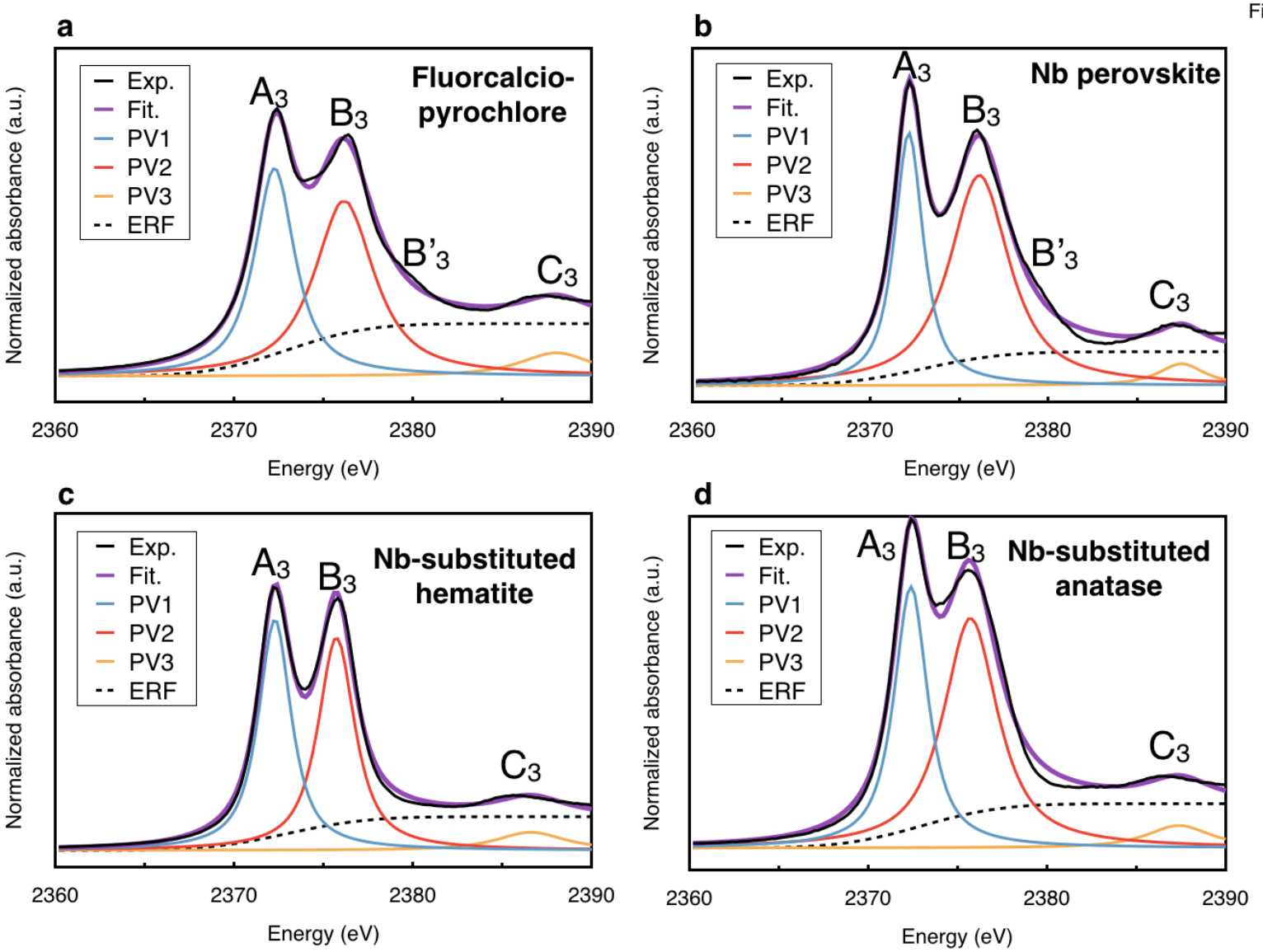
a
Fluorcalcio-pyrochlore
b
Nb perovskite
c
Nb-substituted hematite
d
Nb-substituted anatase
Exp.
Fit.
PV1
PV2
PV3
ERF
A3
B3
B'3
C3
Normalized absorbance (a.u.)
Energy (eV)
2360
2370
2380
2390

Fig. 3

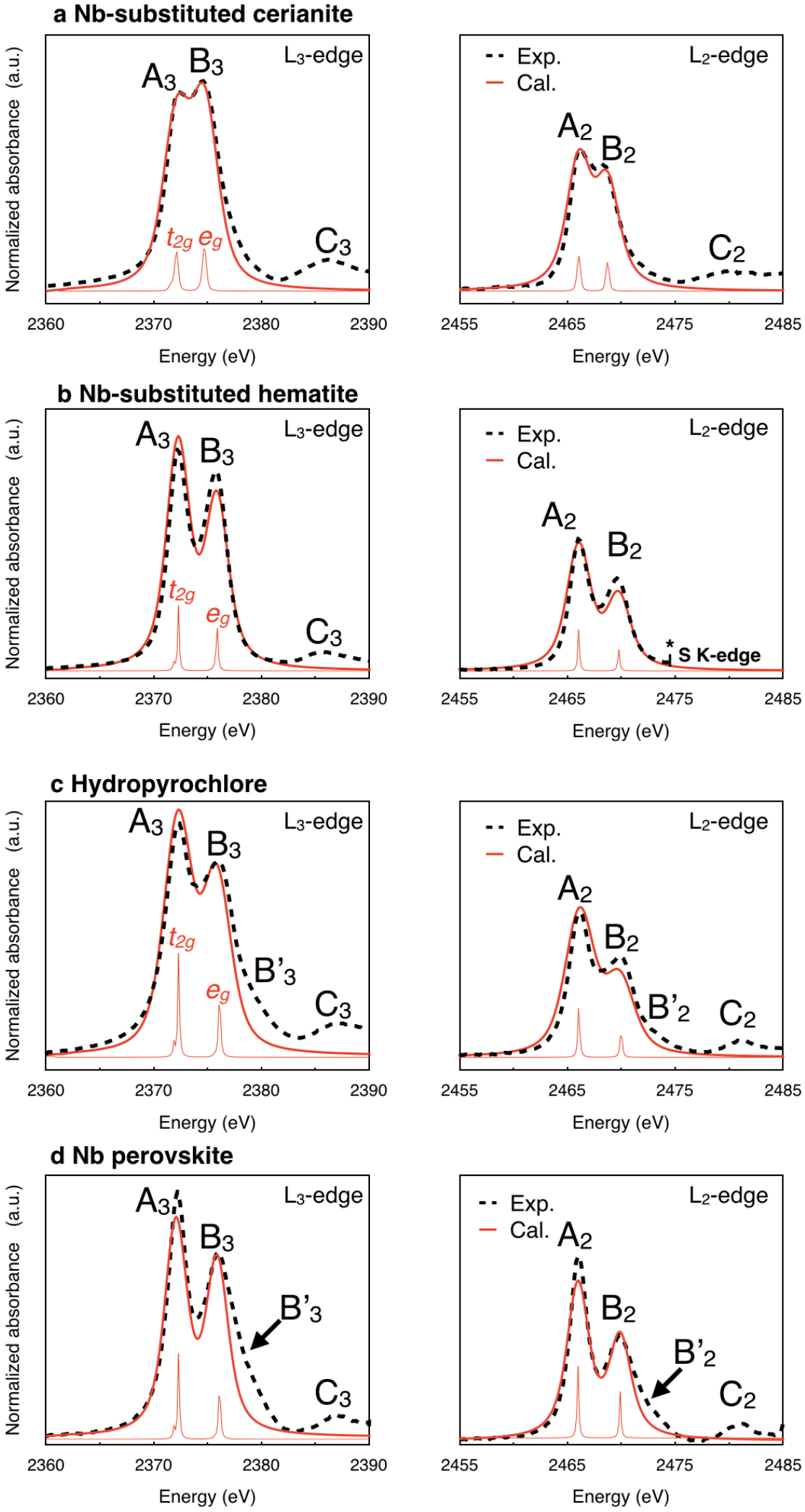
a Nb-substituted cerianite
L3-edge
L2-edge
Exp.
Cal.
A3
B3
C3
t2g
eg
A2
B2
C2
Normalized absorbance (a.u.)
Energy (eV)
2360
2370
2380
2390
2455
2465
2475
2485
b Nb-substituted hematite
* S K-edge
c Hydropyrochlore
B'3
B'2
d Nb perovskite

Fig. 4

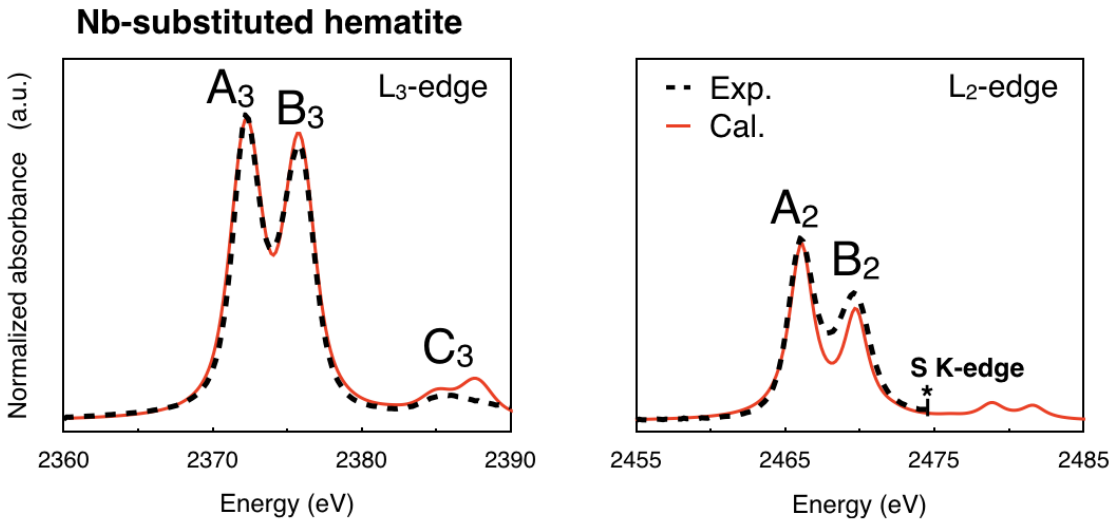
Nb-substituted hematite
Normalized absorbance (a.u.)
A3
B3
C3
L3-edge
2360
2370
2380
2390
Energy (eV)
Exp.
Cal.
L2-edge
A2
B2
S K-edge
*
2455
2465
2475
2485
Energy (eV)

Fig. 5

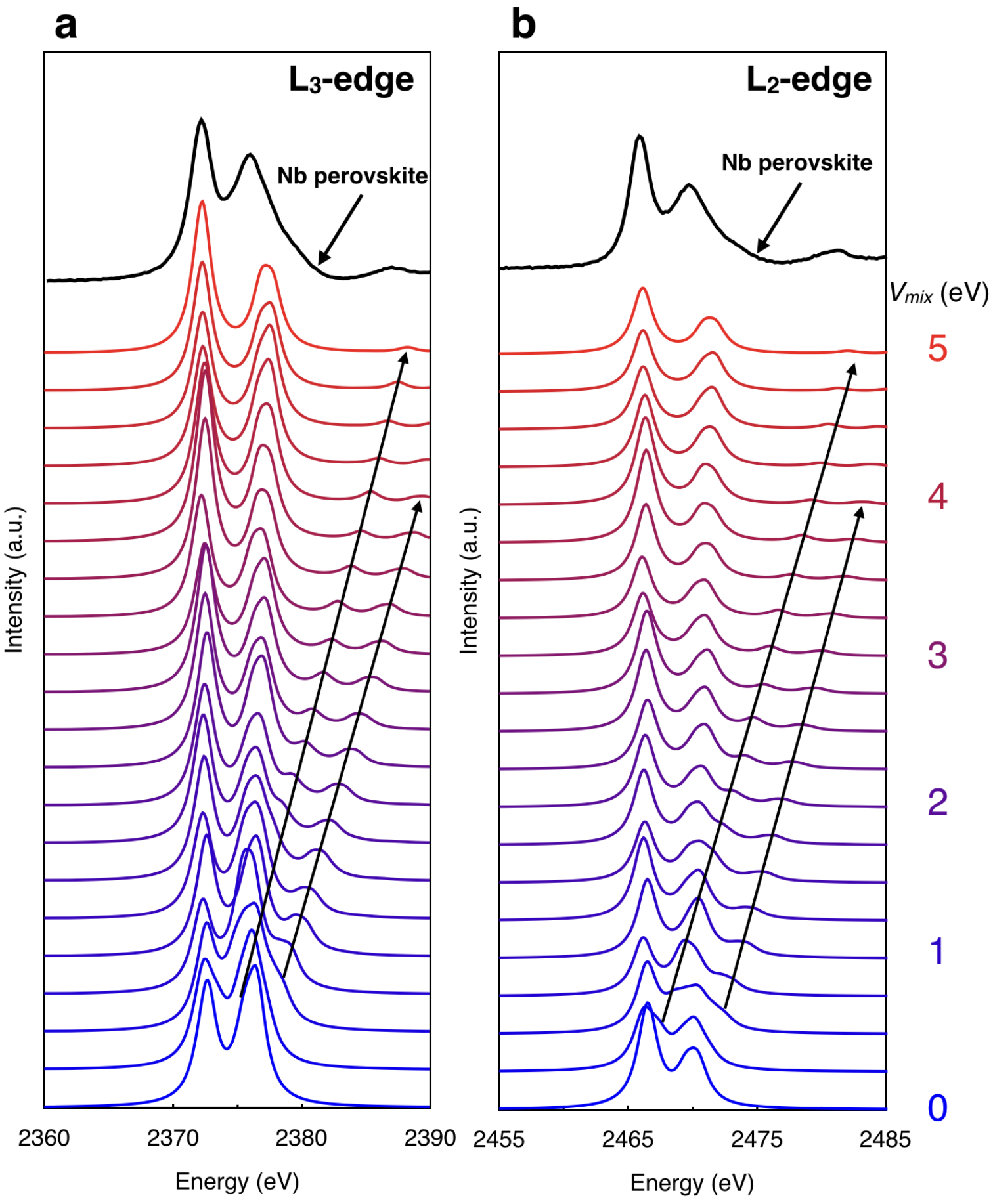
a
L3-edge
Nb perovskite
Intensity (a.u.)
2360
2370
2380
2390
Energy (eV)
b
L2-edge
Nb perovskite
Intensity (a.u.)
2455
2465
2475
2485
Energy (eV)
Vmix (eV)
5
4
3
2
1
0

Fig. 6

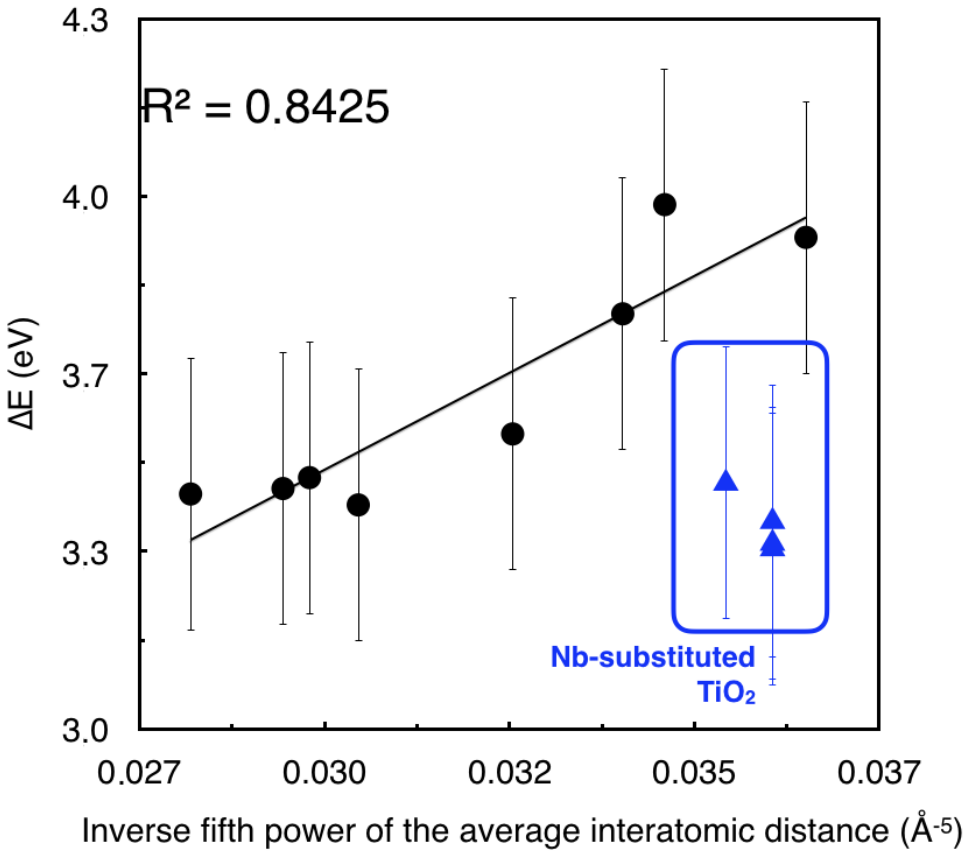
4.3
4.0
3.7
3.3
3.0
ΔE (eV)
R² = 0.8425
Nb-substituted
TiO2
0.027
0.030
0.032
0.035
0.037
Inverse fifth power of the average interatomic distance (Å-5)